

Fracture properties estimation using distributed acoustic sensing recording of guided waves in unconventional reservoirs

Ariel Lellouch¹, Mark A. Meadows², Tamas Nemeth³, and Biondo Biondi¹

ABSTRACT

Perforation shots excite guided waves that propagate in a low-velocity unconventional shale reservoir. They have a frequency content of up to 700 Hz and are dispersive. We have analyzed horizontal crosswell perforation shots recorded by a distributed acoustic sensing (DAS) array. We observe a dramatic influence on the guided SH waves in the form of delayed arrival times, scattering, phase incoherency, and loss of amplitude and frequency, as well as a gradual slowdown of the leaky compressional waves as they propagate through a previously stimulated area. Using a simple geometric analysis of the spatial locations of the distortions in the direct arrivals of the guided SH waves, we can estimate the half-lengths of the induced fractures, which range from 50% to 75% of the distance between the perforated and monitoring wells. Furthermore, we find that the propagation disturbances originate from the middle of the stimulated area. Other diffracted signals, notably from frac plugs, are clearly visible in the data. We report the first large-scale use of DAS records of guided waves. Their potential for high-resolution imaging and inversion of subsurface properties before and after hydraulic stimulation opens new possibilities for the use of seismology in optimizing production from unconventional reservoirs.

INTRODUCTION

Boundary conditions in the subsurface influence elastic and acoustic wave propagation. In general, boundary conditions can be classified into several categories: free surface, rigid surface, and interface (solid-solid, solid-liquid, or liquid-liquid). A variety of

well-known seismic wave types arise from different boundary conditions, such as Rayleigh, Love, Stoneley, and Sholte waves (Aki and Richards, 2002).

Under certain circumstances, boundary conditions can create seismic waveguides. Love waves, for example, are a type of guided wave arising in a layer possessing two particular boundary conditions: a free-surface interface at the top of the layer and a solid-solid interface at the bottom. Waveguides have long been recognized and extensively studied, especially in global seismology (Gutenberg, 1955; Phinney, 1961) and oceanic wave propagation (Pekeris, 1948; Tolstoy and Clay, 1966). Most of the examples of guided waves observed by the scientific community are a result of a free-surface boundary at the top of the waveguide. Other boundary types include the deep seismic waveguide, which is a low-velocity zone embedded within a faster medium with solid-solid interfaces (Krey, 1963). For an isotropic elastic medium, there are two types of guided waves: an SH (Love-type) mode and a P-SV (Rayleigh-type) mode. Their propagation properties differ, but the phase velocity for both is bounded by the shear-wave (S-wave) velocity outside the low-velocity layer.

Although the type boundary condition and specific layer structure control their exact behavior, elastic waveguides share several general properties. If we view guided waves as a summation of waves propagating at different angles in a single layer (Sheriff and Geldart, 1995) and undergoing an idealized, postcritical reflection at the boundaries, there are specific conditions that are required for constructive interference of the different propagating wavefronts. In other words, only specific pairs of wavefronts in the frequency-wavenumber domain can sustain propagation in the waveguide. The combination of such pairs is known as a normal mode. Due to the sinusoidal nature of waves, conditions for constructive interference are temporally cyclic and can be fulfilled by multiple mode types. For the base mode, all frequencies can propagate. In contrast, higher modes have a cutoff frequency below which they cannot exist.

Manuscript received by the Editor 9 December 2019; revised manuscript received 19 May 2020; published ahead of production 15 June 2020.

¹Stanford University, Geophysics Department, Stanford, California 94305-2210, USA. E-mail: arielle@stanford.edu (corresponding author); biondo@stanford.edu.

²Chevron Energy Technology Company, San Ramon, California 94583-2324, USA. E-mail: mmmeadows@chevron.com.

³Chevron Energy Technology Company, Houston, Texas, USA. E-mail: tamas.nemeth@chevron.com.

© 2020 Society of Exploration Geophysicists. All rights reserved.

Another property of guided waves, which is true for all modes, is that they are dispersive. The phase (w/k) and group ($\partial w/\partial k$) velocities depend on the frequency; here, w is the temporal frequency and k is the spatial wavenumber. For a waveguide created by a low-velocity zone bounded by faster ones, phase velocity decreases with frequency. The group velocity behavior is not monotonic. Instead, it has a minimum that occurs at a particular frequency, above which the group velocity increases. The wave type that travels at this minimum group velocity is referred to as the air mode, whose dominant energy occurs because different frequencies propagate at approximately the same group velocity, thus enhancing their collective amplitude (Sheriff and Geldart, 1995).

The normal-mode theory described above accounts only for waves traveling in a perfect waveguide. In such a case, propagating energy is trapped in the waveguide and decays exponentially outside it. However, there is another type of guided wave, known as a leaky mode (Phinney, 1961; Maupin, 1996; Parra et al., 2002). In this case, the waveguide radiates energy into the surrounding medium as body waves in addition to propagating energy within it. These radiation losses are purely elastic and can be calculated by extending normal-mode theory to complex wavenumbers and frequencies. For a low-velocity zone embedded in a faster medium, leaky modes exist as compressional waves (P-waves) that convert at the boundaries. P-waves constructively interfere within the waveguide, but at each reverberation energy is radiated away from the boundaries in the form of S-waves. Therefore, the properties of these waves are strongly influenced by the P-wave velocity of the waveguide, whereas normal modes, which can be SH (Love-type) or P-SV (Rayleigh-type), depend mostly on the waveguide's S-wave velocity.

Elastic guided waves have been used in different seismic studies, such as near-surface property estimation (Eslick et al., 2008; Li et al., 2018), crosswell continuity mapping (Krohn, 1992; Chon et al., 1996), imaging coal seams (Buchanan, 1976), and the seismological study of fault zones (Li et al., 1994). We have previously observed (Lellouch et al., 2019a, 2019b) that perforation shots excite guided waves that propagate in unconventional reservoirs and can be recorded by a downhole distributed acoustic sensing (DAS) system. DAS technology allows for high-resolution spatial and temporal sampling of the seismic wavefield by interrogating an optical fiber (Mateeva et al., 2013; Biondi et al., 2017; Lindsey et al., 2017). Downhole DAS, in particular, has multiple applications, such as microseismic monitoring (Mateeva et al., 2014), earthquake seismology (Lellouch et al., 2019c), vertical seismic profiling (Daley et al., 2016), low-frequency strain measurements (Karrenbach et al., 2018) and fracture hit mapping (Jin et al., 2019). Unlike geophones or accelerometers, DAS measures strain, or the strain rate, parallel to the fiber.

In this study, we claim that guided waves are an efficient tool for detecting and estimating geometric properties of fractured areas. This idea has been proven successful almost four decades ago, using S-waves in a vertical crosswell case (Stewart et al., 1981). We analyze perforation shots in a horizontal crosswell scenario. Both wells are located approximately at the same depth. One of them is equipped with DAS fiber and records data, whereas the other well is perforated. The source well is located between 260 and 280 m away from the well in which the fiber is installed. Guided waves propagate at distances of up to 1 km from the perforation shot location with a very high spatial and temporal frequency content (up to

700 Hz). From a practical point of view, such wavefronts are spatially unaliased at all propagation angles only when recorded with DAS systems. Because the wells are perforated and stimulated using a conventional toe-to-heel schedule, the DAS array records guided waves propagating through previously stimulated and undisturbed parts of the reservoir. We observe two types of guided waves. One is a guided SH mode, whereas the other is a P-type leaky mode. When traveling through previously stimulated areas, the guided SH waves undergo severe changes, which manifest themselves as a combination of a velocity slowdown, scattering, phase incoherency, and loss of amplitude and frequency. The leaky P modes maintain their waveform character but display a measurable slowdown as well. By using geometric considerations, we show how the spatial location of the waveform distortion of the direct guided SH-wave arrivals can be used to estimate the horizontal extent of the fracture system.

We begin by showing perforation shot records and analyzing guided-wave properties in the undisturbed medium. Then, we show the propagation differences between undisturbed and stimulated areas. The clear imprint of the fractures on SH-type guided waves is used in a simple geometric analysis that yields the half-length (HL) (horizontal extent) of the fractures. We also discuss a secondary guided SH-wave that is excited by a tube wave that diffracts off a frac plug. We conclude by showing that P-type leaky modes are significantly less affected by the fractures, despite undergoing a measurable slowdown.

OBSERVED GUIDED WAVES

Data acquisition and processing

The DAS-instrumented well recorded perforation shots from an offset well. The horizontal part of the two wells are approximately parallel and located roughly 260–280 m apart in the area that we analyze. We can reasonably treat them as being located at the same depth, even though variations of a few meters are possible. Acquisition of the offset-well perforation shots occurred more than a month after the recording well had been stimulated. Therefore, we expect that by the time of the crosswell experiment, the stress/strain regime in the reservoir has reached a point of equilibrium. Ambient stress/strain changes due to fluid flow in the induced fractures and natural background fracture network are expected to be close to zero. In the offset well, perforation shots were excited as part of a stimulation program. Available data consist of 11 stages of DAS recordings, each of which contains five shots. The nominal distance between shots is 12 m; however, only 43 shots out of 55 could be identified in the data. Stages are usually separated 6–8 h from one another. Continuous DAS records are difficult to manage in terms of size and computational effort. As a result, only records around times at which a surface microseismic array detected an event were supplied to us. Consequently, some perforation shots were missed. It is theoretically possible to process DAS records and detect missing events using crosscorrelation or matching filter methods, but we do not have access to those data. Furthermore, shot locations along the well are not precisely known to us. Therefore, a certain amount of preprocessing was required to estimate their location.

The first step in estimating the location of the perforations requires choosing a representative perforation-shot record, which is then crosscorrelated in space and time with all other records. Shots can be reasonably aligned using the optimal spatial and temporal

lag. After this initial alignment, we find the optimal apex location of each event assuming perfect left-right symmetry of the leaky P-wave arrivals at the near-apex channels (which are between 50 and 100 m from the apex along the recording well). We thus assume no lateral velocity variation and a symmetric source radiation pattern within this zone.

We analyze propagating guided waves to understand their dispersion properties. A common way to conduct this analysis is in the $f\text{-}k$ domain, which highlights phase and group propagation velocities as a function of frequency. However, to obtain true velocities, the original records cannot be used without further processing; otherwise, an $f\text{-}k$ analysis will measure the apparent velocity along a hyperbolic event trajectory instead of the true velocity of the medium. Therefore, we remap the spatial axis by replacing the channel distance along the fiber with the distance from the source to each DAS channel, assuming that the sources and all DAS channels are located at the same depth. Then, those distances are binned to a 0.25 m interval using linear interpolation at missing locations. These regularized gathers, after an $f\text{-}k$ transformation, show the true phase and group velocities of propagating guided waves.

Guided-wave properties

We show one-sided propagation of a single perforation shot and its $f\text{-}k$ analysis in Figure 1, which proves that leaky P modes and guided SH modes can propagate in a shale waveguide with dispersive properties. The guided P-SV modes can also theoretically propagate in the waveguide but are harder to observe in this configuration. The P-SV guided waves induce particle motion in the vertical axis and along the direction of propagation. The exact distribution between the two depends on the elastic structure and propagating frequency, and it is outside the scope of this study. Because DAS is insensitive to the vertical motion, this component of the guided P-SV wave is invisible. A study of DAS records in VTI anisotropy (Bard et al., 2019) extends isotropic body S-wave behavior to quasi-SV body waves, which disappear from DAS records when the source and receiver are at the same depth. Therefore, the argument about DAS insensitivity to the vertical motion holds for VTI as well. The observability of the horizontal component of the guided P-SV wave, with particle motion along the direction of propagation, depends on the projection of the direction of propagation on the fiber's axis. As a result, the horizontal component of the guided P-SV waves will induce measurable strain only at channels far away from the source, in which the arrivals are broadside to the fiber. Nonetheless, the signal-to-noise ratio is poorer at those channels. In combination with the source radiation patterns discussed later, this explains why P-SV guided waves cannot be directly observed in the field data.

The propagation group velocity that we observe, which is approximately 2 km/s, matches the fast S-wave velocity in the sonic logs acquired along the horizontal portion of the

monitoring well (see Lellouch et al., 2019b, for the logs). It is known that for VTI anisotropy, the fast mode along the horizontal direction is the SH polarization, whose particle displacement is in the horizontal plane containing the DAS fiber. Mixed S-P or P-S guided modes, which are not predicted by theory, are not present in the data, as shown in Figure 1. However, we can see additional events of leaky P and guided SH waves. They propagate at relatively low frequencies and have higher phase velocities than the main guided waves and appear as short branches above the principal modes in the $f\text{-}k$ domain (see Figure 1). Detailed phase-velocity analysis shows that they are also dispersive. We are not yet certain, but we suspect that these are two distinct base modes with different properties due to the reservoir structure.

The leaky P-waves have an interesting spectral property. There is a significant energy decrease between 250 and 400 Hz in their $f\text{-}k$ spectra. This gap can also be observed in the time-domain data. For P-waves, low and high frequencies appear as distinct branches and no coherent energy exists between them. However, for the wavenumber range at which the leaky P-waves are the weakest, SH waves are at their maximum. Therefore, the effect of the DAS gauge length (Dean et al., 2017) cannot be the cause of this phenomenon. The gauge length manifests itself as a wavenumber notch, so it should appear for the P- and S- velocities, although at different frequencies. From the wave propagation modeling that we have conducted, this spectral gap is consistent with leaky-mode propagation. Although guided waves display a balanced power spectrum, leaky modes tend to concentrate their energy only in certain parts of the spectrum. We have confirmed this observation with

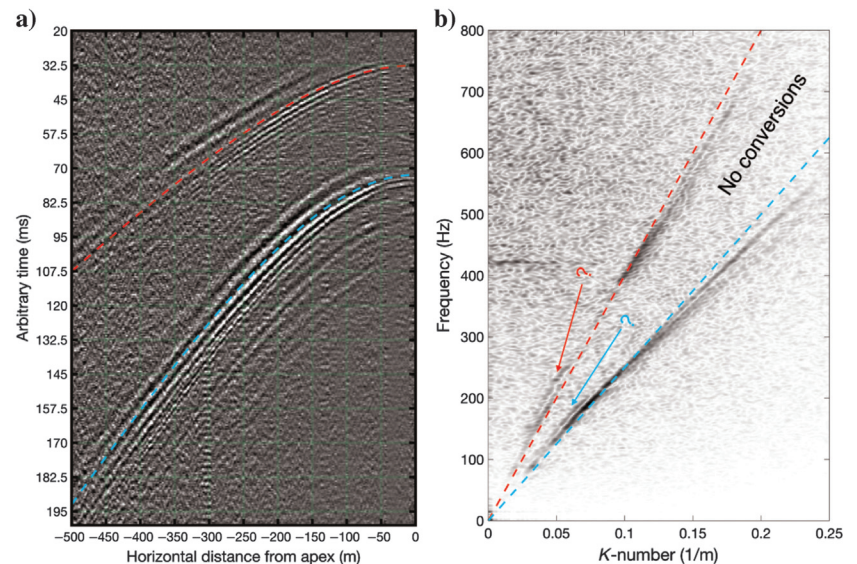


Figure 1. One-sided propagation of a crosswell perforation shot (from Lellouch et al., 2019b). Seismograms, ordered by horizontal distance from the source apex along the recording well, are shown in (a). Hyperbolic moveouts, computed with $V_P = 4$ km/s and $V_S = 2.5$ km/s and a distance of 266 m between wells, are overlaid in red and cyan, respectively. The dispersive nature of the data is evident, but a hyperbolic moveout is a good approximation of their kinematics. In (b), we show an $f\text{-}k$ analysis of the data after source-channel distance regularization. The same velocities ($V_P = 4$ km/s and $V_S = 2.5$ km/s) are plotted with matching colors. The dispersive nature that was previously observed is evident here. Other events are visible for P (the red arrow) and S (the cyan arrow) modes, which cannot be unequivocally identified in the time domain. Mixed P-S or S-P guided modes, whose velocity would differ from V_P and V_S and would appear roughly where “no conversions” is marked, are not present.

a modification of the semianalytical solutions proposed by [Buchen and Ben-Hador \(1996\)](#).

It is also worth mentioning why there is no apparent notch due to the DAS gauge length. The data was acquired with 1 m channel spacing and 10 m gauge length. The wavelengths we observe range from 4 to 100 m. We thus do not expect spatial aliasing, but the gauge length can influence recorded signals. The gauge length manifests itself as notches at certain wavenumbers over all frequencies ([Dean et al., 2017](#)). In its simplest form, the wavenumber response due to a gauge length (GL) is $\sin(\pi \cdot GL)/\pi \cdot GL$; we thus expect notches at $k = n/GL$, where n is an integer. The reason we do not observe clear notches is due to the geometric configuration. Arrivals roughly follow a hyperbolic moveout. Therefore, k , which depends on the apparent velocity along the fiber, is not constant. As a result, different portions of the array vary in their spectral response to a given source. When we simultaneously analyze the entire record, we are effectively blending different responses, each with notches at different locations. The total response, which is a linear summation of individual responses, does not contain clear notches. Computing the exact response of the array is not within the scope of this study, but it can easily be done by summing data from individual fiber segments after accounting for the different apparent velocities.

The recorded signal also depends on the source mechanism. We compare recorded data to the expected source radiation pattern from a perforation in a fluid-filled borehole ([Fehler and Pearson, 1984](#)) after rotation to a horizontal crosswell geometry and adaptation to DAS-equivalent strain data. The resulting source radiation pattern for isotropic body-wave propagation predicts no SV (particle motion along the vertical axis) energy. In other words, even if vertical geophones had been deployed instead of DAS, no SV body-wave arrivals would have been recorded. Nonetheless, as we previously stated, guided-wave propagation is different than that of body waves. The fact that the source is probably generating weak SV energy, combined with the lower sensitivity of DAS to P-SV guided waves discussed earlier, is probably the reason we do not observe clear P-SV arrivals in the field data.

In our study, we observe guided-wave propagation in an anisotropic layered medium. Nonetheless, we can support our approximation based on Fehler and Pearson's ([1984](#)) predictions for a uniform isotropic layer. Guided waves are confined to the low-velocity reservoir, whose velocity is quite uniform before stimulation; therefore, our constant-velocity assumption is acceptable. Naturally, this assumption breaks with induced fractures, but we observe propagation in the undisturbed reservoir first. In the field data, source-channel distances exceed 260 m and the reservoir is approximately 15 m thick. By taking the horizontal component of the anisotropic velocity, we can reasonably approximate guided-wave propagation as isotropic because most of the propagating energy is indeed confined to the horizontal plane, given that only postcritical angles exist in the waveguide. Finally, geometric spreading will vary for guided waves. Instead of spherical spreading, it will be approximately cylindrical ([Aki and Richards, 2002](#)) because the propagation is principally horizontal and confined to the waveguide. For leaky waves, there is an additional loss that we do not take it into account. However, initial modeling tests show that the degree of loss is not a significant factor for the geologic conditions at this location.

The point-source amplitude radiation pattern for P and S body waves in a homogeneous isotropic medium, measured along the

borehole (A_P and A_S , respectively), is a function of the angle ϕ between the propagation raypath and the axis of the source borehole, and the source-receiver distance R ([Fehler and Pearson, 1984](#)):

$$\begin{aligned} A_P &\sim \frac{1}{\lambda + \mu} \cdot \frac{1}{R} \cdot [\lambda + \mu - \mu \cdot \cos^2(\phi)], \\ A_S &\sim \frac{1}{\mu} \cdot \frac{1}{R} \cdot \sin(2\phi). \end{aligned} \quad (1)$$

Here, λ is Lamé's first parameter and μ is the shear modulus of the medium. For $\phi = 0^\circ$, propagation is along the source well. The S-wave amplitude, in this case, is zero, as we have observed in previous studies ([Lellouch et al., 2019b](#)). The hyperbolic apex from a crosswell acquisition is obtained at $\phi = 90^\circ$. Several modifications are required to adapt these equations to a DAS measurement of guided waves. First, the propagation is cylindrical and not spherical; thus, R should be replaced by \sqrt{R} . We then apply this amplitude correction to the recorded field data based on the estimated source location and its distance to each receiver. Next, we project the radiation amplitude onto the measurement lines and apply a spatial derivative to obtain strain. After applying these corrections, we obtain

$$\begin{aligned} A_P &\sim \frac{1}{\lambda + \mu} \cdot k \cdot \cos(\phi) \cdot [\lambda + \mu - \mu \cdot \cos^2(\phi)], \\ A_S &\sim \frac{\lambda + \mu}{\mu} \cdot k \cdot \sin(\phi) \cdot \sin(2\phi), \end{aligned} \quad (2)$$

where k is the spatial wavenumber. Because the apparent velocity changes with location along the fiber, special care is needed when interpreting the crosswell data spectrum. To account for different wavenumbers, we normalize the data by multiplying them by k^{-1} in the f - k domain. In Figure 2, we show field data after this correction, as well as the analytical amplitudes from equation 2 after the effect of k has been removed. Note that a horizontal distance of 266 m along the monitoring well is equivalent to 45° . This analysis shows that, up to angles of approximately 30 degrees for P-waves and 40° for S-waves, the predicted radiation pattern adequately explains the low-frequency component of the field data. At larger angles, the P- and S-wave amplitudes undergo a sharp decline that cannot be explained by this approach. In addition to the limitations stated earlier, we also do not take into account elastic scattering and anelastic dissipation, which could be a possible cause for these discrepancies. However, our approach yields a stable first-order prediction of the dynamic behavior of guided waves generated by perforation shots, and field data amplitudes generally follow the predicted analytical curves.

MEASURING STIMULATION EFFECTS

SH-wave distortions and their properties

The stimulation treatment at the offset well starts at the toe and moves toward the heel. Therefore, for most perforation shots, we can simultaneously observe propagation through stimulated and undisturbed areas. We reiterate that the recording well had been perforated and stimulated several weeks before the offset well and is producing while the offset well is being stimulated. Thus, no zone between the two wells is genuinely undisturbed. Nevertheless, we

can readily observe in the DAS data the change induced by the stimulation of the offset well.

In Figure 3, we show perforation shots from different locations along the well. The stimulated area has a pronounced effect on the guided SH-wave propagation, whereas the leaky P-waves appear relatively unaltered. The sensitivity of S-waves to fluid-filled fractures in terms of velocity and attenuation is a well-studied topic (Schoenberg and Sayers, 1995; Tan et al., 2014). The effect of the stimulated area on wave propagation, manifested as a velocity slowdown, amplitude[↓] and frequency loss, and scattering, greatly varies between perforation shots, indicating variability in the induced fracture systems between stages. However, time-dependent effects could be playing a significant role in causing this variability. The temporal difference[↑] between the last stimulation of one stage and the first perforation of the next stage varies. Therefore, we sample the reservoir at different points in time as it continually adjusts to a new stress/strain equilibrium. There is clear evidence of fracture influence for distances of up to approximately 250 m from the apex along the recording well. For channels located farther away, the wavefield seems to propagate without distortion. The high-frequency source content, along with the high spatial resolution of the recording array, open the possibility of directly characterizing the fracture system for individual stages. The data shown in Figure 3 cover approximately 300 m of stimulation over two days of operation.

In this study, we follow a simple, approximate approach that does not aim to explain the complex disturbed SH-wave behavior fully. Instead, it focuses on the channel location at which the distortion in the direct SH-wave arrivals appears. For a given stage, five perforation shots are conducted within a few minutes. Consequently, waves generated by perforation shots within the same stage can be assumed to encounter the same properties of the reservoir. However, roughly six to eight hours pass between adjacent stages, and the subsurface properties cannot be assumed constant within this time period. Therefore, we analyze all perforation shots from each stage separately (five at most). In Figure 4, we show all of the shots for one particular stage. Although variability exists between the different perforations within a given stage, we focus on the distance from the apex along the recording well at which the distortion of the SH-wave direct arrivals is first visible. This example shows that as the perforation moves away from the stimulated area, the distance from the apex at which the first-arrival distortion is detected increases. We conducted this analysis for all other stages, and the behavior is similar. This observation indicates that a certain feature at a consistent location within the stimulated area is causing the disturbance.

For some of the perforation shots, we also observe a secondary signal whose apex is roughly aligned with the spatial position of the first-arrival distortion. Because such events are invisible for most perforation shots, it is challenging to analyze them consistently. However, because they are temporally separated from the first arrivals at all channels, they cannot be explained by a simple point diffraction model. We discuss the reason later in the “Secondary signals” section.

Fracture estimation

Previous studies have described how time-lapse DAS recordings can be used to estimate vertical fracture growth (Bakku et al., 2014; Binder et al., 2018; Titov et al., 2019). They are based on time-lapse

surface sources recorded by a horizontal or vertical DAS array. In this study, we estimate the horizontal fracture growth. In Figure 5, we show a simple geometric explanation of the stimulated area’s effect. We assume that the abrupt change in the SH-wave direct arrivals at a certain recording channel is due to an interaction with the edge of the stimulated area. Naturally, the real shape of the stimulated area is likely not rectangular. We can express the geometric relationship between the features denoted in Figure 5 by the following linear equation:

$$\text{Offset} = \frac{L}{HL} \cdot D + \frac{D_0 L}{HL}. \quad (3)$$

Therefore, estimating the HL of the developing fractures amounts to plotting offset as a function of D for each stage and finding the best linear fit. We can also estimate D_0 from the intercept of the linear fit. However, for most stages, we have data for only three or four shots out of five and we do not know which shots within each stage are

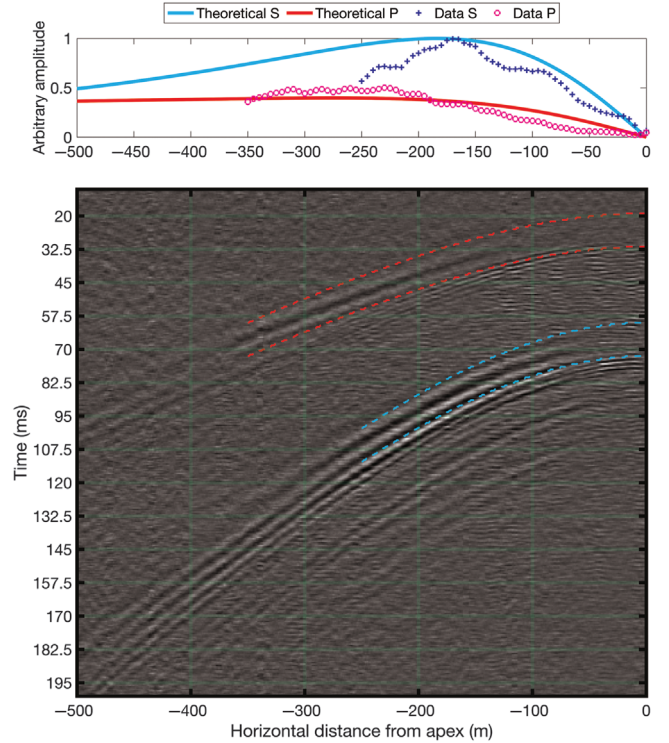


Figure 2. Recorded crosswell data compared to the analytical source radiation pattern from the DAS source. Data are plotted as a function of horizontal distance along the monitoring well. They have been corrected for guided-wave geometric spreading and wavenumber effects and are displayed without any additional scaling. The analytical radiation patterns for P- and S-waves are plotted above the seismograms (red, P; cyan, S), together with the field data amplitudes (blue cross, P; magenta circle, S). These amplitudes are measured within the plotted corridors (dashed red, P; dashed cyan, S), which have been chosen because they include lower frequencies that are less prone to anelastic losses. For each channel, the amplitude is estimated as the maximum of the data envelope within the corridor. We similarly compute the amplitudes in a noise window preceding the P event, average those values along all channels, and subtract the mean noise amplitude from the amplitude computed in the P and S corridors. As a result, the plotted amplitudes are close to zero at short horizontal distances.

missing. The term D_0 is only applicable to the first observed shot, which may be farther away from the stimulation zone if the first shot in the stage was not recorded.

We show the results of the suggested analysis in Figure 6. Only stages with four or more shots are displayed. For the HL estimation, we compute the possible errors. We assume no error in D but add a random Gaussian error with a 10 m standard deviation to the picked value of D_0 at which the direct SH-wave distortion first appears. This procedure is repeated 1000 times, and D_0 is estimated for each virtual data set. Then, we choose the 5% and 95% confidence intervals as representative of the possible error due to picking one shot.

The HL estimation varies between stages. This fluctuation cannot be explained solely by estimation errors. Therefore, we conclude that there are physical differences in fracture behavior across the various stages. The mean estimated HL is approximately 165 m. The distance between the wells is 260–280 m. The offset and monitoring wells were stimulated. Because the distance between the wells was designed for optimal production, the estimated HL is consistent with field development plans. Any value less than 130–140 m would mean that not all of the reservoir volume is stimulated, given the well spacing. However, to assure full recoverability, the well spacing is designed assuming that not all of the stimulated volume is being produced (Barree et al., 2005). Our average estimation

of the HL amounts to a 20% difference between the two, which is a reasonable value in well-spacing design.

As we previously mentioned, the estimation of D_0 suffers from inherent uncertainty because we are missing a shot in most of the perforation stages of the offset well. However, because we analyze only stages with four or five shots, the possible error is bounded by the distance between shots in a stage, which is approximately 12 m. In addition, D_0 can only be overestimated. By looking at the distances from the first shot (the horizontal axis in Figure 6a), the sources appear to be equally spaced. We thus conclude that either the first or last shot in each stage (except stage #6, in which all five shots were recorded) is missing. From Figure 6b, the mean value of D_0 is approximately 43 m. Because for all stages but one D_0 may be overestimated by the distance between subsequent shots in the stage, which is 12 m, we conclude that the true average D_0 lies between 33 and 43 m. For the only stage that contains all of the shots, we get a value of 38 m. The distance from the last shot in the previous stage is approximately 12 m. The size of a stage, consisting of five shots, is 48 m. Therefore, its middle lies 24 m away from the last shot in the stage, or 36 m away from the first shot in the subsequent stage. The mean D_0 value that we estimate is very close to this distance. This indicates that the SH-wave disturbance probably occurs near the central area of the previous

stage's stimulated volume. However, it could also be due to the disturbance arising from the cumulative effect of propagating through a series of fractures.

Secondary signals

Recorded data also contain diffracted signals originating from tube waves reflecting on frac plugs installed to isolate stages during stimulation, as observed by Seher et al. (2014) and Bergery et al. (2017). The plugs are positioned between adjacent stages, but only the most recent plug can act as a diffractor because tube waves cannot propagate past it and reach older plugs. In previous studies, we observed strong tube waves propagating in the perforated well with a velocity of approximately 1475 m/s. The waves reflect and diffract from the plug. In Figure 7, we show a simple traveltime analysis that demonstrates that the plugs act as S-wave diffractors. In other words, tube waves generated by the perforation shot travel within the stimulated well and are then converted to S-waves at the plug. We do not observe a significant conversion to P-waves. The diffracted S-waves propagate as guided waves, as is evident by their dispersive nature — low frequencies propagate faster than higher frequencies. The diffraction traveltimes T are computed by

$$T = \frac{X_S - X_{PLUG}}{V_W} + \frac{\sqrt{L^2 + (X_{REC} - X_{PLUG})^2}}{V_S}, \quad (4)$$

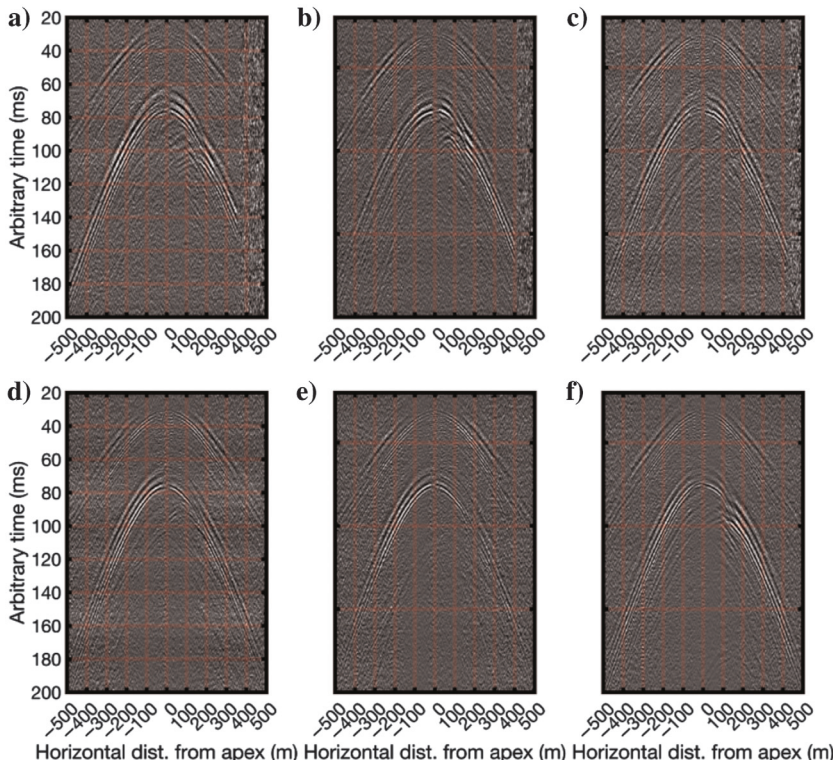


Figure 3. Perforation shots taken from different stages. Shots are moving away from the toe in (a-f). DAS channels are ordered by horizontal distance from the estimated apex along the recording well. Positive distances correspond to the toe-ward side of the monitoring well. For some of the shots in part (a)-(c), the end of the fiber is reached within the recorded range and noisy channels appear. The difference between the left (undisturbed) and right (stimulated) sides is evident for the S-wave arrivals. However, the nature of the S-wave disturbance varies, and can appear as a slowdown, amplitude and frequency loss, multiple scattering, and more. Consistent changes in the P-wave arrivals cannot be directly observed.

where X_S is the perforation location along the stimulated well, X_{PLUG} is the location of the frac plug along the stimulated well, $V_W = 1475 \text{ m/s}$ is the tube-wave speed, $L = 279 \text{ m}$ is the distance between wells for the given stage, and X_{REC} is the channel location along the recording well. The term V_S is the guided SH-wave velocity, which is frequency dependent because guided waves are dispersive. We apply an additional 5 ms constant shift to improve the match to the field data. This empirical correction is possibly a result of a traveltime delay related to the conversion from tube wave to subsurface SH wave. The frequency content of the diffracted SH waves is lower than that of the direct SH waves, with a maximum frequency of approximately 300 Hz, as opposed to 550–600 Hz for the direct SH waves. Bergery et al. (2017) observe that the diffracted events are P-waves, with significantly lower frequency content but greater energy than the direct P arrivals. Seher et al. (2014) find that tube-to-shear diffractions are stronger and are more clearly visible in the recorded data than tube-to-P diffractions, as we have observed. However, they find that the frequency content of the direct arrival is an order of magnitude greater than in the plug-diffracted waves. It is difficult to apply these results to our study, which involves a different recording geometry and guided-wave, rather than body-wave, propagation. However, because our data set is richer in spatial resolution and frequency content, we are certain that, in our specific case, tube-to-shear conversions are more dominant than tube-to-P conversions, and the frequency difference between direct and diffracted events is not as large as observed by Seher et al. (2014).

We now revisit the diffractions discussed earlier (shown in Figure 4). These diffractions appear to originate within the stimulated area of the previous stage because their apex spatially coincides with the onset of the disturbance of the direct SH waves. It is thus natural to speculate that the tip of the horizontally propagating fractures is the cause of such diffractions. From our estimation of the fracture HL and horizontal location relative to the perforation shots, we can properly position the diffractor at the fracture tip. In our analysis, we assume a representative propagation velocity of 2800 m/s for low-frequency guided SH waves.

Figure 8 shows that predicted diffraction moveouts do not match field data. First, the recorded diffracted signal appears later than the predicted event and does not intersect the direct SH-wave arrival. The two events would be expected to intersect at location (1) along the monitoring well, where the diffracted and direct paths coincide. The observed lag can be explained by a

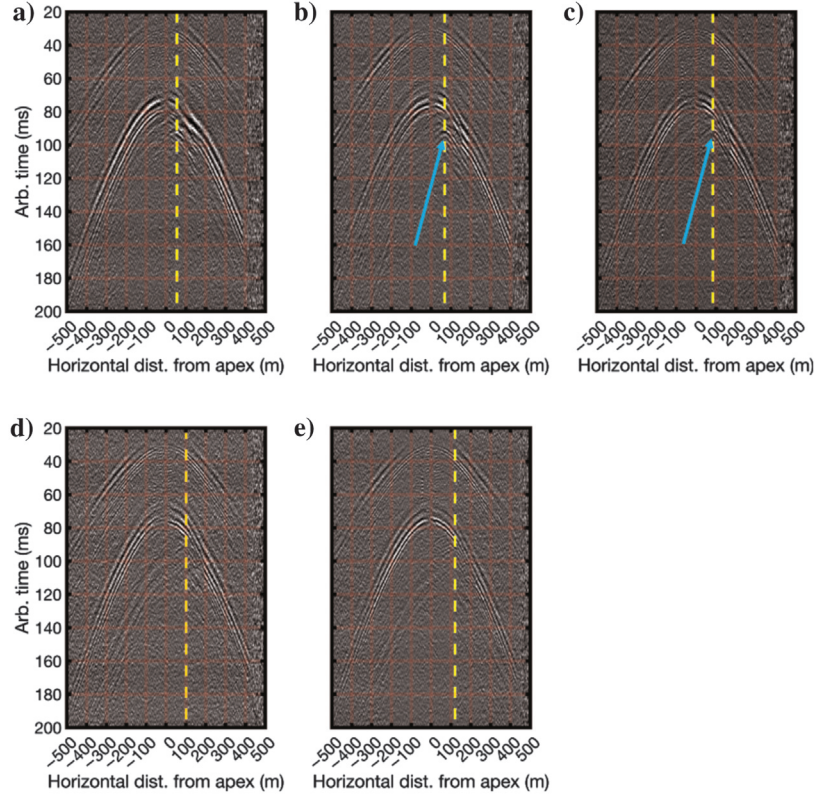


Figure 4. All perforation shots for one particular stage, with the DAS channels ordered by distance from the estimated apex along the recording well. Traces are individually balanced. From (a) to (e), shots are moving away from the previous stage, and positive distances correspond to the toe-ward side of the monitoring well. The nominal distance between adjacent shots is 12 m. The distance from the apex at which the distortion of direct SH-wave arrivals is first visible is marked by a dashed yellow line. This distance increases as the shots move farther from the stimulated area of the previous stage. Diffracted signals that appear to originate from the location of the first-arrival distortion are present. The diffraction apices are marked in panel (b and c) by a cyan arrow.

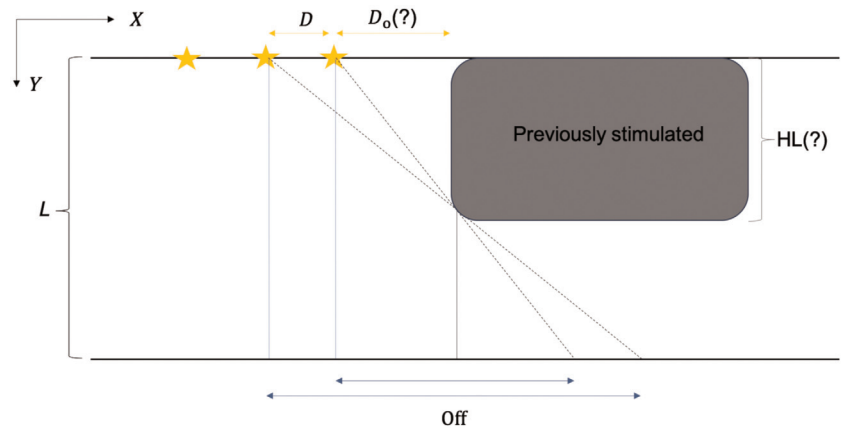


Figure 5. Geometric interpretation of the stimulated-zone effect in map view. Shots, denoted by yellow stars, are moving away from the disturbed area (schematically marked in gray) from right to left. The first shot is at a distance D_0 , and subsequent shots are at a distance nD from the first shot, where n is an integer. The HL is the fracture length in the disturbed area is HL, and the distance between the wells is L . At two shots, the horizontal distance along the recording well is Off, which we don't detect the direct SH-waves distortion is marked in blue arrow. A blue arrow indicates propagation is through an undisturbed medium and the signal appears continuous. The shown parameters are HL and D_0 .

significant slowdown within the diffraction zone, or by a slower P-SV guided wave that undergoes conversion to SH at the diffraction location. However, a slowdown would affect both events equally and therefore cannot explain the discrepancy. In the latter case, of conversion between different S modes, the strong anisotropy (approximately 30% S-wave splitting) of the reservoir can adequately explain the time lag of the diffracted signal. Given the perforation-shot radiation pattern, however, P-SV events are expected to be significantly weaker than SH events. Furthermore, conversions be-

tween P-SV and SH waves occur only in complex structures that likely do not apply to this simple reservoir geometry. Another shortcoming of the point-diffractor approach is that it predicts a difference between the diffraction apex location (2) and the location at which direct S-waves undergo a disturbance (1). In the field data, they seem to spatially coincide, indicating that the diffraction zone does not radiate energy expected from a point diffractor. Given the limited quality and extent of the recorded diffractions in our data, we are unable to conduct a reliable investigation of this phenomenon; therefore, we leave a more complete analysis to further studies.

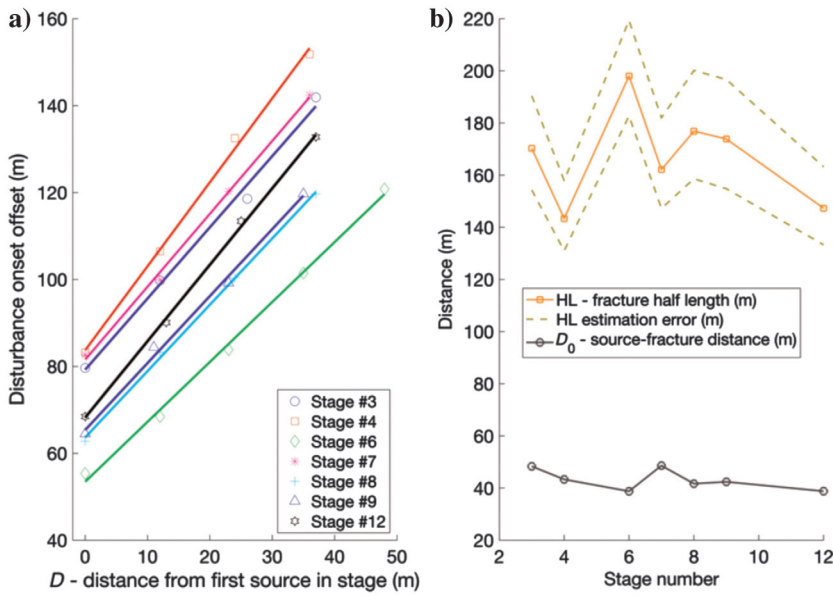


Figure 6. (a) Best fits of offset versus D for different stages. We display the stages that have four or five recorded shots. Each stage is denoted by a different color. (b) Estimated fracture HL and D_0 . HL is plotted in orange, and its error (5% and 95% confidence intervals) is in dashed dark yellow. The term D_0 is in gray. There is variability between the different stages that cannot be explained by measurement errors.

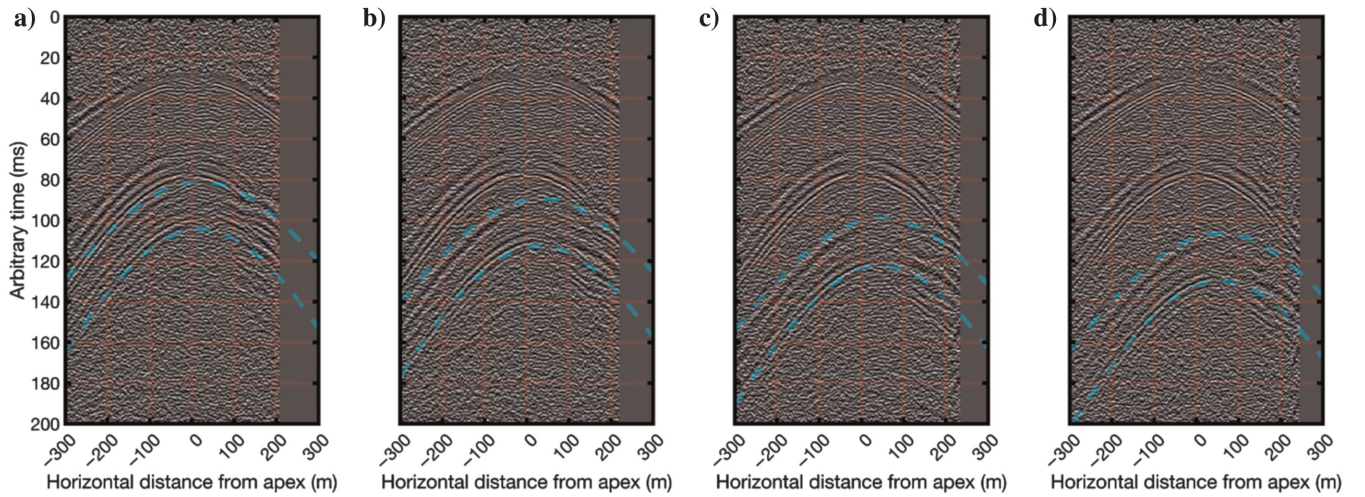


Figure 7. Frac plug diffraction analysis. Several shots from the same stage are displayed with DAS channels ordered by the horizontal distance from the event apex along the recording well. Positive distances correspond to the toe-side of the monitoring well, where channels at the end of the fiber are zeroed. The apex of the diffraction signal shifts to the right as the shot moves progressively away from the plug from (a) to (d). The dashed lines show the computed moveouts of the diffracted signals (equation 4) for $V_S = 3000 \text{ m/s}$ (per line, low frequencies) and $V_S = 2400 \text{ m/s}$ (per line, high frequencies). These match the traveltimes of the diffracted events.

consistent delay in the P-wave arrivals in the stimulated area. This delay accumulates with distance, and there is no sharp break as for the SH waves. By design, the difference in arrival times between the left and right branches of the event hyperbola should be zero at distances within 100 m of the apex. For distances of 100–200 m, the lag builds up toward a 1 ms delay. This delay is stable until a 300 m distance is reached, after which the quality deteriorates, resulting in more extreme values that also inconsistently change signs. Qualitatively, the delay buildup follows the black line shown in Figure 9, which represents the onset locations of the direct SH-wave distortions. This behavior is not surprising because propagation up to that distance is undisturbed. When S-waves encounter the fracture system, the effect is immediate due to the presence of fluid-filled fractures. However, for P-waves, the effect is more gradual because the fluid component merely slows down the propagating wave rather than abruptly stopping it at the fracture face (Binder et al., 2018). We cannot unequivocally conclude that the delay is consistent at longer horizontal distances because such delays cannot be measured. If they were measurable, they could result from poor correlation quality rather than a physical property of the medium.

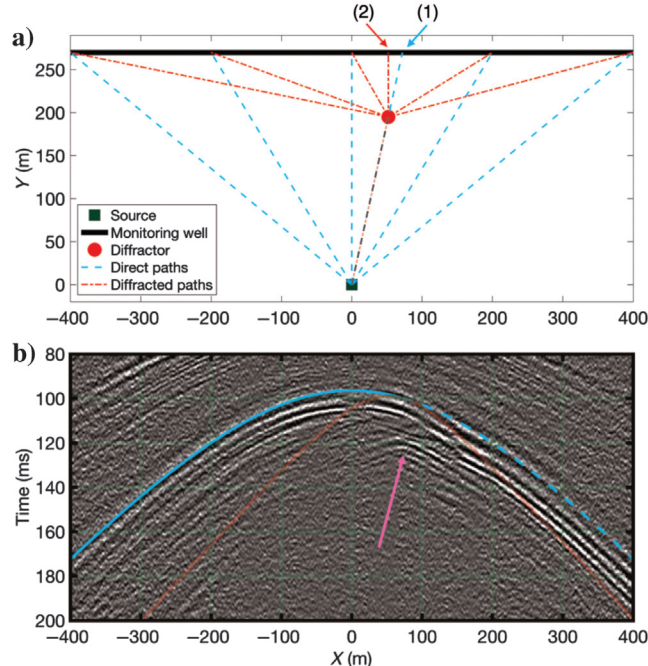


Figure 8. A naive point diffractor interpretation. (a) The geometric setup in map view, indicating the source (green rectangle), monitoring well (black line), and point diffractor (red circle) representing the zone of the fractured zone. The direct (dashed cyan line) and diffracted (dashed-dotted line) rays are overlaid. The diffraction apex is expected at (2), whereas the disturbance of the direct SH arrivals occurs at (1). (b) Recorded data (gray) containing reflection (the apex indicated by the purple arrow). Overlay constant velocity moveouts assuming $V_S = 2800$ m/s computed for the direct (cyan) and diffracted (red) arrivals. For the direct arrivals, the dashed part denotes propagation through the stimulated area. The theoretical moveouts do not agree with the field data because the diffraction apex (the magenta arrow) is shifted in space and time compared to its predicted location.

DISCUSSION

Perforation shots generate guided waves that propagate through the subsurface while maintaining a very high frequency content. They are dispersive, and their propagation velocities, whether phase or group, vary with frequency. Thanks to their confinement to the shale formation, they undergo a weaker geometric spreading than do body waves. As such, frequencies of 600–700 Hz can easily propagate for distances of hundreds of meters. Even secondary events, originating from tube waves diffracting off frac plugs, are visible at long distances. Guided waves sample the subsurface in a 2.5D fashion because they repeatedly bounce between the shale formation boundaries while primarily propagating horizontally. The shortest dimension in this acquisition scenario is the width of the waveguide, which is the height of the shale formation. Consequently, guided-wave studies are less likely to suffer from out-of-plane events, which are often a nuisance in vertical crosswell analysis using body waves (Schuster, 1996). Any energy propagating in the shale reservoir at a subcritical angle and exiting the waveguide in the early propagation stages is very unlikely to return

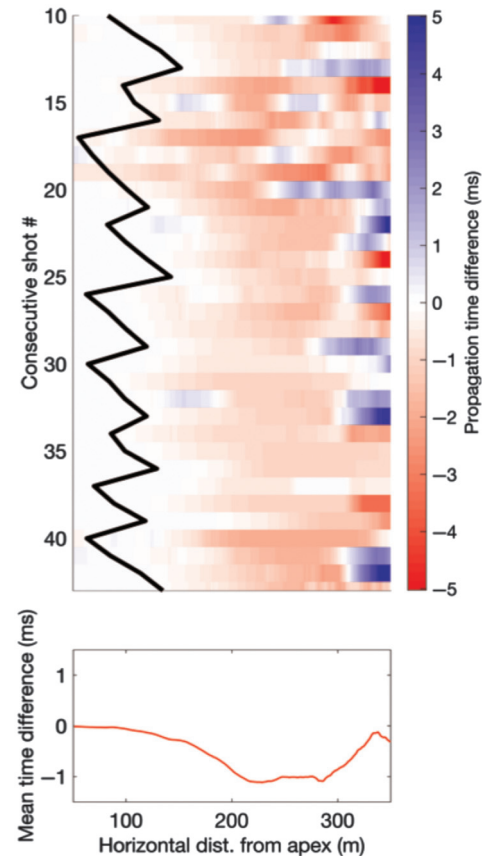


Figure 9. Estimated P-wave slowdowns due to stimulation. For each perforation shot, we plot the time delay at different horizontal distances from the apex. Negative (red) values indicate that propagation through the previously stimulated area lags relative to propagation through the undisturbed part. The area between 50 and 100 m is used to estimate the apex location and should have a lag close to 0 ms by design, which, except for shot #19, is indeed the case. The black line indicates where the direct S-wave distortion was picked. The bottom plot shows the mean lag for different distances from the apex, computed across all perforation shots.

to it. For this to happen, the wavefronts would have to reenter the formation at a postcritical angle to be trapped within it. Mode conversions from S to P could facilitate such a transmission across the boundary, but it is nonetheless very unlikely for flat-lying structures such as the ones in our study area because any waves leaving the reservoir would very likely continue to propagate at subcritical angles. Therefore, we do not observe any reflection/diffraction events from outside the shale layer.

Fully understanding the complexity of SH-waves propagating through a previously stimulated area demands a wave-equation imaging or inversion approach. We do not see how ray approximations can explain the complexity of the records in terms of disturbed SH-wave behavior and secondary colocated diffractions, if present in the records. However, the simplified analysis that we present in this paper leads to an approximate location of the  of the reservoir causing the perturbations in the observed  wave direct arrivals. For a complete wave-equation analysis, additional information will be needed. First, accurate source locations must be supplied by the operator. In addition, a better representation of the source function in terms of a temporal wavelet and, possibly, directivity, is critical.

An essential component of the SH-wave analysis is that at channels far away from the source apex, the recorded wavefield seems to propagate undisturbed. In other words, the dramatic effect of the interaction with the fluid-filled fractures disappears. Although there may be some residual slowdown, we were not able to observe it consistently. Any fracture propagation model explaining these observations would have to account for undisturbed SH-wave propagation at wide angles. One explanation is that fractures splay in the horizontal direction as they propagate away from the injection point; therefore, waves propagating close to the well are less affected by the fractures than waves propagating in areas farther away from the injection points and closer to the recording well. Another possibility is based on the assumption that the preceding stimulation of the fiber-instrumented well has created open, propellant-filled fractures. Stimulation of the offset well reinjects fluid into those fractures, which are far away from the stimulated offset well. Therefore, only near-apex guided-wave propagation will be influenced by these fractures. Guided waves reaching the more distant channels do not travel through these fractures and are, therefore, not affected. Finally, a waveform-healing approach may be used to explain our observations. Close to the disturbances, we see destructive interference patterns in the recorded wavefronts. For channels located farther away, the wavefronts regain their continuous character.

We believe that there would be many benefits to recording seismic data by DAS in the offset well, in addition to the  well. First, three different subsurface models could be constructed completely undisturbed, after stimulation and production of the monitoring well, and after stimulation of the offset well. In the current acquisition, we can only observe propagation effects due to stimulation of the offset well. Furthermore, we assume layered 1D geology and detect stimulation-induced effects by comparing propagation in different areas. This approximation is a potential pitfall because there are preexisting geologic heterogeneities that are not due to the stimulation of the offset well. Having two DAS-instrumented wells would allow for near-perfect removal of the signal due to initial geologic conditions from the stimulation-induced changes.

CONCLUSION

Perforation shots excite guided waves that can propagate through a low-velocity shale formation. The DAS acquisition system adequately records them. Guided waves have a broad frequency content (up to 700 Hz) and are dispersive. Due to the source mechanism of perforation shots and the DAS acquisition geometry, guided SH waves dominate crosswell records.  wave diffractions originating from  waves scattering off frac plug are also visible. As guided SH waves propagate through previously stimulated areas, they undergo severe disturbances. The spatial location at which we can first observe distortions of the first guided SH wave arrivals varies with the location of the perforation shots. In some of the records, secondary colocated diffractions are also visible. By first-order analysis of the spatial location of the distortion of the direct  wave arrivals, we estimate the HL of the stimulated area and its distance from the different perforation shots. Results indicate that the primary imprint on the guided SH wave originates from the center of the stimulated area from the previous stage. We also observe a consistent, gradual slowdown of the leaky P-waves traveling through the stimulated area. Interestingly, for recording channels located far away from the source apex, the SH-wave propagation reverts to its initial undisturbed state. We hypothesize that this behavior could be caused by horizontal splaying of the fractures, but more field observations and complex fracture propagation models would be required to validate or reject this idea. In this study, we can prove only the existence of guided waves and their properties in this specific geologic setting. We encourage readers to return to the DAS recordings of perforation shots, look for signs of such guided waves, and inform our community of their findings.

ACKNOWLEDGMENTS

We thank Chevron Energy Technology Company for providing data and permission to publish this study. We are specifically grateful to K. Nihei, M. Craven, and D. Bevc for their helpful comments and discussions. S. Horne helped us in the early research stages. We used a GPU finite-difference implementation of the wave equation, developed by E. Biondi, G. Barnier, and S. Farris, to study guided- and leaky-wave properties. This study was supported in part by the Israeli Ministry of Energy under the program for postdoctoral scholarships in leading universities.

DATA AND MATERIALS AVAILABILITY

Data associated with this research are confidential and cannot be released.

REFERENCES

- Aki, K., and P. G. Richards, 2002, Quantitative seismology: University Science Books.
- Baird, A., A. Stork, S. Horne, G. Naldrett, M. Kendall, J. Wookey, A. Clarke, and J. Verdon, 2019, Modelling of fibre-optic DAS response to microseismic arrivals in anisotropic media: 81st Annual International Conference and Exhibition, EAGE, Extended Abstracts, We_R09_08, doi: [10.3997/2214-4609.201901244](https://doi.org/10.3997/2214-4609.201901244).
- Bakku, S. K., P. Wills, M. Fehler, J. Mestayer, A. Mateeva, and J. Lopez, 2014, Vertical seismic profiling using distributed acoustic sensing in a hydrofrac treatment well: 84th Annual International Meeting, SEG, Expanded Abstracts, 3796–3800, doi: [10.1190/segam2014-1559.1](https://doi.org/10.1190/segam2014-1559.1).
- Barree, R. D., S. A. Cox, M. L. Dobson, and J. V. Gilbert, 2005, Closing the gap: Fracture half length from design, buildup, and production analysis: SPE Production and Facilities, **20**, 274–285, doi: [10.2118/84491-PA](https://doi.org/10.2118/84491-PA).

- Bergery, G., Z. Zhang, J. Du, D. Diller, T. Shuck, and B. Fish, 2017, The plug drum effect, or why your microseismic events may not be where you think they are: SPE/AAPG/SEG Unconventional Resources Technology Conference, 2701–2710.
- Binder, G., A. Titov, D. Tamayo, J. Simmons, A. Tura, G. Byerley, and D. Monk, 2018, Time delays from stress-induced velocity changes around fractures in a time-lapse DAS VSP: 88th Annual International Meeting, SEG, Expanded Abstracts, 5328–5332, doi: [10.1190/segam2018-2998082.1](https://doi.org/10.1190/segam2018-2998082.1).
- Biondi, B., E. Martin, S. Cole, M. Karrenbach, and N. Lindsey, 2017, Earthquakes analysis using data recorded by the Stanford DAS Array: 87th Annual International Meeting, SEG, Expanded Abstracts, 2752–2756, doi: [10.1190/segam2017-17745041.1](https://doi.org/10.1190/segam2017-17745041.1).
- Buchanan, D. J., 1976, The propagation of attenuated SH channel waves: Geophysical Prospecting, **26**, 16–28, doi: [10.1111/j.1365-2478.1978.tb01575.x](https://doi.org/10.1111/j.1365-2478.1978.tb01575.x).
- Buchen, P. W., and R. Ben-Hador, 1996, Free-mode surface-wave computations: Geophysical Journal International, **124**, 869–887, doi: [10.1111/j.1365-246X.1996.tb05642.x](https://doi.org/10.1111/j.1365-246X.1996.tb05642.x).
- Chon, Y. T., W. Turpening, S. Rutherford, and M. Parchman, 1996, Reservoir continuity logging using connectivity mapping while drilling: The Leading Edge, **15**, 203–208, doi: [10.1190/1.1437296](https://doi.org/10.1190/1.1437296).
- Daley, T. M., D. E. Miller, K. Dodds, P. Cook, and B. M. Freifeld, 2016, Field testing of modular borehole monitoring with simultaneous distributed acoustic sensing and geophone vertical seismic profiles at Citronelle, Alabama: Geophysical Prospecting, **64**, 1318–1334, doi: [10.1111/1365-2478.12324](https://doi.org/10.1111/1365-2478.12324).
- Dande, S., R. S. Stewart, M. T. Myers, L. Hathon, and N. Dyaur, 2019, Elastic properties of propped and unpropped Eagle Ford shale and 3D-printed fractured models under iso-static stress: SPE/AAPG/SEG Unconventional Resources Technology Conference, 115.
- Dean, T., T. Cuny, and A. H. Hartog, 2017, The effect of gauge length on axially incident P-waves measured using fibre optic distributed vibration sensing: Geophysical Prospecting, **65**, 184–193, doi: [10.1111/1365-2478.12419](https://doi.org/10.1111/1365-2478.12419).
- Eslick, R., G. Tsolfias, and D. Steeples, 2008, Field investigation of Love waves in near-surface seismology: Geophysics, **73**, no. 3, G1–G6, doi: [10.1190/1.2901215](https://doi.org/10.1190/1.2901215).
- Fehler, M., and C. Pearson, 1984, Cross-hole seismic surveys: Applications for studying subsurface fracture systems at a hot dry rock geothermal site: Geophysics, **49**, 37–45, doi: [10.1190/1.1441559](https://doi.org/10.1190/1.1441559).
- Gutenberg, B., 1955, Channel waves in the Earth's crust: Geophysics, **20**, 283–294, doi: [10.1190/1.1438141](https://doi.org/10.1190/1.1438141).
- Jin, G., K. Mendoza, B. Roy, and D. G. Buswell, 2019, Machine learning-based fracture-hit detection algorithm using LFDAS signal: The Leading Edge, **38**, 520–524, doi: [10.1190/tle38070520.1](https://doi.org/10.1190/tle38070520.1).
- Karrenbach, M., S. Cole, A. Ridge, K. Boone, D. Kahn, J. Rich, K. Silver, and D. Langton, 2019,  AS microseismic, strain and temperature monitoring during hydraulic fracturing: Geophysics, **84**, no. 1, D11–D23, doi: [10.1190/geo2017-0396.1](https://doi.org/10.1190/geo2017-0396.1).
- Krey, T. C., 1963, Channel waves as a tool of applied geophysics in coal mining: Geophysics, **28**, 701–714, doi: [10.1190/1.1439258](https://doi.org/10.1190/1.1439258).
- Krohn, C. E., 1992, Cross-well continuity logging using guided seismic waves: The Leading Edge, **11**, 39–45, doi: [10.1190/1.1436887](https://doi.org/10.1190/1.1436887).
- Lellouch, A., B. Biondi, S. Horne, M. A. Meadows, and T. Nemeth, 2019a, DAS observation of guided waves in a shale reservoir generated by perforation shots: 89th Annual International Meeting, SEG, Expanded Abstracts, 943–947, doi: [10.1190/segam2019-3212667.1](https://doi.org/10.1190/segam2019-3212667.1).
- Lellouch, A., S. Horne, M. A. Meadows, S. Farris, T. Nemeth, and B. Biondi, 2019b, DAS observations and modeling of perforation-induced guided waves in a shale reservoir: The Leading Edge, **38**, 943–947, doi: [10.1190/tle38110858.1](https://doi.org/10.1190/tle38110858.1).
- Lellouch, A., S. Yuan, Z. Spica, B. Biondi, and W. L. Ellsworth, 2019c, Seismic velocity estimation using passive downhole distributed acoustic sensing records: Examples from the San Andreas Fault Observatory at Depth: Journal of Geophysical Research, Solid Earth, **124**, 6931–6948, doi: [10.1029/2019JB017533](https://doi.org/10.1029/2019JB017533).
- Li, J., S. Hanafy, and G. Schuster, 2018, Wave-equation dispersion inversion of guided P waves in a waveguide of arbitrary geometry: Journal of Geophysical Research, Solid Earth, **123**, 7760–7774, doi: [10.1029/2018JB016127](https://doi.org/10.1029/2018JB016127).
- Li, Y.-G., K. Aki, D. Adams, A. Hasemi, and W. H. K. Lee, 1994, Seismic guided waves trapped in the fault zone of the Landers, California, earthquake of 1992: Journal of Geophysical Research, Solid Earth, **99**, 11705–11722, doi: [10.1029/94jb00464](https://doi.org/10.1029/94jb00464).
- Lindsey, N. J., E. R. Martin, D. S. Dreger, B. Freifeld, S. Cole, S. R. James, B. L. Biondi, and J. B. Ajo-Franklin, 2017, Fiber-optic network observations of earthquake wavefields: Geophysical Research Letters, **44**, 792–799, doi: [10.1002/2017GL075722](https://doi.org/10.1002/2017GL075722).
- Mateeva, A., J. Lopez, J. Mestayer, P. Wills, B. Cox, D. Kiyashchenko, Z. Yang, W. Berlang, R. Detomo, and S. Grandi, 2013, Distributed acoustic sensing for reservoir monitoring with VSP: The Leading Edge, **32**, 3–7, doi: [10.1190/tle32101278.1](https://doi.org/10.1190/tle32101278.1).
- Mateeva, A., J. Lopez, H. Potters, J. Mestayer, B. Cox, D. Kiyashchenko, P. Willis, S. Grand, K. Hornman, B. Kuvshinov, W. Berlang, Z. Yang, and R. Detomo, 2014, Distributed acoustic sensing for reservoir monitoring with vertical seismic profiling: Geophysical Prospecting, **62**, 679–692, doi: [10.1111/1365-2478.12116](https://doi.org/10.1111/1365-2478.12116).
- Maupin, V., 1996, The radiation modes of a vertically varying half-space: A new representation of the complete Green's function in terms of modes: Geophysical Journal International, **126**, 762–780, doi: [10.1111/j.1365-246X.1996.tb04701.x](https://doi.org/10.1111/j.1365-246X.1996.tb04701.x).
- Parra, J. O., C. L. Hackert, A. W. Gorody, and V. Korneev, 2002, Detection of guided waves between gas wells for reservoir characterization: Geophysics, **67**, 38–49, doi: [10.1190/1.1451322](https://doi.org/10.1190/1.1451322).
- Pekeris, C. L., 1948, Theory of propagation of explosive sound in shallow water: Geological Society of America Memoir, 1–116.
- Phinney, R. A., 1961, Leaking modes in the crustal waveguide — Part 1: The oceanic PL wave: Journal of Geophysical Research, **66**, 1445–1469, doi: [10.1029/jz066i005p01445](https://doi.org/10.1029/jz066i005p01445).
- Schoenberg, M., and C. M. Sayers, 1995, Seismic anisotropy of fractured rock: Geophysics, **60**, 204–211, doi: [10.1190/1.1443748](https://doi.org/10.1190/1.1443748).
- Schuster, G. T., 1996, Resolution limits for crosswell migration and travel-time tomography: Geophysical Journal International, **127**, 427–440, doi: [10.1111/j.1365-246X.1996.tb04731.x](https://doi.org/10.1111/j.1365-246X.1996.tb04731.x).
- Seher, T., S. Rondenay, and H. Djikpesse, 2014, Tube wave to shear wave conversion at borehole plugs: Geophysical Prospecting, **62**, 540–551, doi: [10.1111/1365-2478.12095](https://doi.org/10.1111/1365-2478.12095).
- Sheriff, R. E., and L. P. Geldart, 1995, Exploration seismology: Cambridge University Press.
- Stewart, R. R., R. M. Turpening, and M. N. Toksoz, 1981, Study of a subsurface fracture zone by vertical seismic profiling: Geophysical Research Letters, **8**, 1132–1135, doi: [10.1029/GL008i011p01132](https://doi.org/10.1029/GL008i011p01132).
- Tan, Y., C. Chai, and T. Engelder, 2014, Use of S-wave attenuation from perforation shots to map the growth of the stimulated reservoir volume in the Marcellus gas shale: The Leading Edge, **33**, 1090–1096, doi: [10.1190/tle33101090.1](https://doi.org/10.1190/tle33101090.1).
- Titov, A., G. Binder, Y. Liu, J. Simmons, A. Tura, G. Byerley, and D. Monk, 2019, Observations and modeling of scattered waves from hydraulic fractures in a DAS VSP experiment in the Permian Basin: 89th Annual International Meeting, SEG, Expanded Abstracts, 4849–4853, doi: [10.1190/segam2019-3203933.1](https://doi.org/10.1190/segam2019-3203933.1).
- Tolstoy, I., and C. S. Clay, 1966, Ocean acoustics: McGraw-Hill.

Queries

1. Please provide postal code for the affiliation 3. 
2. We have changed Karrenbach et al. (2019) to Karrenbach et al. (2018) to match the reference list. Is this correct? 
3. Please expand the term "VTI" at first mention. 

Funding Information

The following agencies have been identified as providing funding for your article. Please review the information carefully. If any changes are required, please submit those along with your other corrections to this article.

- Stanford Exploration Project (SEP) Sponsors
- Israeli Ministry of Energy

